Infrared Laser-Induced Amyloid Fibril Dissociation: A Joint Experimental/Theoretical Study on the GNNQQNY Peptide

Takayasu Kawasaki, Viet Hoang Man, Yasunobu Sugimoto, Nobuyuki Sugiyama, Hiroko Yamamoto, Koichi Tsukiyama, Junmei Wang, Philippe Derreumaux, Phuong H. Nguyen

Infrared Laser Induced Amyloid Fibril Dissociation: A Joint Experimental/Theoretical Study on the GNNQQNY peptide

Takayasu Kawasaki,[*,†] Viet Hoang Man,[‡] Yasunobu Sugimoto,[¶] Nobuyuki Sugiyama,[§] Hiroko Yamamoto,[§] Koichi Tsukiyama,[†] Junmei Wang,[‡] Philippe Derreumaux,[*,∥,⊥] and Phuong H. Nguyen[*,#]

IR-FEL Research Center, Research Institute for Science and Technology, Organization for Research Advancement, Tokyo University of Science, 2641 Yamazaki, Noda, Chiba 278-8510, Japan

, Department of Pharmaceutical Sciences, School of Pharmacy, University of Pittsburgh, Pittsburgh, PA 15213, USA

, Synchrotron Radiation Research Center, Nagoya University, Furo-cho, Chikusa, Nagoya 464-8603, Japan

, Aichi Synchrotron Radiation Center, 250-3 Minamiyamaguchi-cho, Seto-shi, 489-0965, Japan

, Laboratory of Theoretical Chemistry, Ton Duc Thang University, Ho Chi Minh, Vietnam, Faculty of Pharmacy, Ton Duc Thang University, Ho Chi Minh, Vietnam

, and CNRS, Université de Paris, UPR9080, Laboratoire de Biochimie Théorique, Paris, France ; Institut de Biologie Physico-Chimique, Fondation Edmond de Rothschild, PSL Research University, Paris, France

E-mail: kawasaki@rs.tus.ac.jp; philippe.derreumaux@tdtu.edu.vn; nguyen@ibpc.fr

Abstract

Neurodegenerative diseases are usually characterized by plaques made of well-ordered aggregates of distinct amyloid proteins. Dissociating these very stable amyloid plaques is a critical clinical issue. In this study, we present a joint mid-infrared free electron laser experiment/non-equilibrium molecular dynamics simulation to understand the dissociation process of a representative example GNNQQNY fibril. By tuning the laser frequency to the amide I band of the fibril, the resonance takes place and dissociation is occurred. The calculated and observed wide-angle X-ray scattering profiles and secondary structures before and after laser irradiation being identical, we can propose a dissociation mechanism with high confidence from our simulations. We find that dissociation starts in the core of the fibrils by fragmenting the intermolecular hydrogen bonds and separating the peptides and then propagates to the fibril extremities leading to the formation of unstructured expanded oligomers. We suggest that this should be a generic mechanism of the laser-induced dissociation of amyloid fibrils.

Introduction

The self-assembly of amyloid proteins into amyloid fibrils is a major hallmark of neurodegenerative diseases such as Alzheimer's and Parkinson disease.[1,2] Amyloid fibrils *in vitro* and *in vivo* display a cross β-structure with β-sheets stabilized by intermolecular backbone hydrogen bonds.[3,4] Their characteristics make them insoluble and extremely stable.[5,6] A large variety of experimental techniques have been used to reveal the aggregation process. Atomic force microscopy[7,8] and ultrasonic force microscopic[9] can record the assembly process by time-lapse imaging. Two-

*To whom correspondence should be addressed
†IR-FEL Research Center
‡University of Pittsburgh School of Pharmacy
¶Synchrotron Radiation Research Center
§Aichi Synchrotron Radiation Center
‖Laboratory of Theoretical Chemistry
⊥Faculty of Pharmacy
#CNRS

dimensional infrared spectroscopy with site-specific isotope labelling can monitor the amyloid formation pathways at a residue-specific resolution and real timescales.[10–12]

In spite of extensive research, many small molecules or antibodies targeting the Aβ protein of 39-43 amino acids retard aggregation kinetics, all clinical trials have had negative outcomes for Alzheimer's disease (AD).[13–15] Whether the encouraging phase 1 clinical data using the aducanumab antibody binding to monomers and small oligomers of amyloid-β protein are further supported remains to be determined.[16] All these molecules target one specific molecular event: small oligomers, primary nucleation process, fibril elongation and fragmentation, and surface-catalyzed mechanism,[17] and each of these events can induce toxicity by amyloid-oligomers interactions with cellular membrane and proteins or unknown mechanisms.[18]

Albeit there is no correlation between the number of amyloid deposits and the severity of Alzheimer's disease, limiting secondary nucleation by destabilizing the highly stable amyloid plaques is an important issue and several methods are possible.[19]Chemicals such as guanidine hydrochloride or dimethyl sulfoxide[20] cannot be used as they are very toxic. *In vitro* experiments have shown that protein modification by including a molecular photoswitch, such as azobenzene chromophore, followed by light excitation can switch the system from favorable to unfavorable aggregates, resulting in protein disassembly.[21–27] Goto and colleagues have shown that ultrasonication accelerates the depolymerization of fibrils into monomers *in vitro*.[28,29] Leinenga et al. were able to remove cerebral amyloid deposition in the mouse brain by using repeated scanning ultrasound.[30] On the theoretical side, Okumura and colleagues have demonstrated that under ultrasonication the formation of empty space around the hydrophilic residues causes collapse of the fibril.[31] We demonstrated that the cavitation of bubbles under ultrasound also induces fibril dissociation.[32]

Another approach to disassembly amyloid fibrils is to use a free-electron laser (FEL) tuned to the amide I band (1600 - 1700 cm^{-1}). Using FEL with specific oscillation characteristics of a picosecond pulse structure, a tunable wavelength within infrared frequencies and a high photon density, Kawasaki et al. were able to dissociate amyloid fibrils of lysozyme, insulin and short peptide fragments of the thyroid and calcitonin hormones.[33–37] To obtain an appropriate theoret-

ical description of the FEL-induced experiments, we developed a laser-induced non-equilibrium molecular dynamics (NEMD) simulation method[38–41] and applied it to the dissociation of fibrils made of 5-mers of the U-shape Aβ17-42 peptide and 5-mers of the left-handed β solenoid 79-residue HET-s protein.[42] Samples containing amyloid fibrils, DNA duplexes and globular proteins (such as prion and acylphosphatase) were also considered and the NEMD simulations showed that the surrounding protein and DNA molecules were hardly affected, demonstrating therefore frequency laser selectivity for dissociation.

While FEL coupled to various microscopy methods can provide morphology and secondary structure evolution after a given time of laser irradiation, these experiments have limited spatial and temporal resolutions preventing a full understanding of the molecular mechanism of amyloid fibril dissociation. On the other hand, this information can be obtained from all-atom NEMD simulations, but the laser intensity and irradiation time used in simulations are much higher and shorter, respectively than the values used in experiment. It is therefore important to determine whether the process of the laser-induced conformational dissociation of the fibril obtained by experiments and simulations is similar.

To address this issue, we present a joint experimental/computational study on the laser-induced dissociation of the amyloid fibril made of the 7-residue GNNQQNY peptide, a fragment of the N-terminal of the yeast prion protein Sup35 known to form amyloid fibrils by its own.[43–45] The structural characteristics of the fibril and the irradiated fibril are analyzed by several experimental techniques, including Thioflavine T (ThT) binding assay, scanning electron microscopy (SEM), synchrotron radiation-based X-ray scattering, that is wide angle X-ray scattering (WAXS), and FT-infrared microscopy. The conformational conversion upon laser excitation is followed by atomistic NEMD simulations in explicit solvent. It is important to note that the present NEMD simulation based on a sample of 200 peptides and an irradiation time of 500 ps goes one step ahead of our early NEMD study on the same peptide using a 32-mer and 50 ps.[42] Overall, this work shows the high complementary of mid-infrared FEL and all-atom NEMD simulation to provide an amyloid fibril dissociation mechanism at an atomistic level.

Methodologies

Experiments

Materials

The GNNQQNY peptide (freeze dried sample after chromatographic preparation, more than 85% purity) was purchased from PH Japan (Hiroshima). Thioflavine T was purchased from Nacalai Tesque (Kyoto, Japan).

Preparation of the fibril

The peptide was dissolved in 20% acetic acid (pH 3−4) and stocked at –30°C (concentration: 10 mg/mL). For the fibrillation, the stock solution (100 μL) was incubated at 37°C for 20 h. The solution (about 10 μL) containing the aggregate was applied to the irradiation experiments.

IR-FEL experiment

The irradiation was performed by using mid-infrared FEL oscillation system at Tokyo University of Science.[46] The experimental setup is schematically shown in Figure 1. The time structure of the laser is composed of micro-pulse and macro-pulse, in which micro-pulse has a duration of 2 pico-second (ps), and its interval is 350 ps, and macro-pulse has several thousands of micro-pulses, and its duration is 2 μs. The oscillation frequency of macro-pulse is 5 Hz. The irradiation power was as usual 9-10 mJ per one macro-pulse, and the beam diameter was focused to about 0.4 mm using BaF_2 lens for the irradiation, and the irradiation time was set to 3 min (about 900 macro-pulses).

Thioflavine T (ThT) binding assay

The peptide solution is added to the reagent solution (25 μM) to total 100 μL volume, and the fluorescent intensity is measured at 492 nm using an excitation wavelength of 450 nm on a microplate reader Varioskan Flash (Thermo Fisher Scientific). The measurement was performed 10 times and the plot data was described as mean.

SR-based X-ray scattering

The X-ray scattering experiments are performed using the beamline BL8S3 at the Aichi Synchrotron Radiation Center, Aichi, Japan. The wavelength of X-ray was 0.15 nm and the sample-to-specimen length is 45 cm for measurements. The scattering patterns are recorded by the use of R-AXIS imaging plate (Rigaku, Japan). Each exposure time of X-ray was 600 s. The peptide sample (approximately 1 mg) dried after the FEL irradiation is incorporated into a glass capillary tube of 1mm in diameter, and the capillary is set in the vertical direction for the X-ray scattering experiments.

Infrared microscopy

The FT-IR measurement is performed using an infrared microscope (IRT-7000, Jasco Co., Tokyo) equipped with Fourier transform infrared spectrometer (FT/IR-6100, Jasco Co., Tokyo). The peptide solution of ten micro litre is added on the stainless-steel slide base and dried under atmosphere. The resulting powder adsorbed on the metal surface is observed by the infrared microscopy with 16x Cassegrain lens. Infrared absorption spectra from 1000 to 4000 cm^{-1} are acquired from 12 or 14 square fields (100 x 100 μm each) on the deposited powder by reflection mode. Those spectra are averaged, and the averaged absorption intensities are used for the analysis of the secondary structures. The proportion of secondary structures is estimated by measuring the peak intensity from 1600 to 1700 cm^{-1} after the deconvolution of the amide I band.

Scanning-electron microscopy (SEM)

We used FE-SEM Supra40 scanning electron microscope (Carl Zeiss) and the procedure for analysis is described in Ref.[37] In brief, the suspension of the amyloid fibril was added on a glass slide base and dried under atmosphere. The sample spot of ca. 5 mm in diameter was surrounded by thin conductive copper tapes. The surface of the sample was observed using an acceleration voltage of 5.0 kV.

Molecular dynamics simulation

Modeling the fibril state

Our initial model was taken from the micro-crystal unit cell structure of the GNNQQNY fibril (PDB entry 1YJP),[44] consisting of 8 β-sheets, each sheet of 18 GNNQQNY peptides (Figure 2A). This structure of 136 peptides is solvated into an octahedral box with a volume of 2257 nm^3, containing 67565 water molecules, resulting in 224 095 atoms. We use the AMBER-F99SB-ILDN force field[47] to model the peptide and the TIP3P water model[48] to describe the solvent. This force field was found to provide a good balance in terms of structures, thermodynamics and kinetics for other amyloid peptides.[49,50] The system was neutralized by adding Na^+ cations. Starting from this structure, a short simulation of 1 ns is carried out in the NPT ensemble followed by a 100 ns NVT simulation at 310 K, employing the GROMACS program.[51] Here, the bond lengths with hydrogen atoms are fixed with the SHAKE algorithm[52] and the equations of motion are integrated with a time step of 2 fs using the leapfrog algorithm. The electrostatic interactions are calculated using the particle mesh Ewald method and a cutoff of 1.1 nm.[53] A cutoff of 1.2 nm is used for the van der Waals interactions. The nonbonded pair lists are updated every 10 fs. Temperatures are controlled by the Berendsen thermostat.[54]

Taking the last structure of the trajectory, we calculated the secondary structures using the STRIDE program.[55] Here, the eight STRIDE structures are grouped into four structures: β-sheet = extended + bridge, helix = α-helix + 3_{10}-helix, turn = turn + bend, and coil = coil + PII-helix. The populations from MD are 72% of β-sheet and 28% of coil. These values are, however, different from the FT-IR populations of our sample prior to FEL experiment consisting of 68% of β-sheet, 14% of turn, 18% of coil and no helix (see below). This is not surprising as we know that the experimental sample must contain fibrils with a low concentration of free monomers. As a result, we place randomly 68 disordered GNNQQNY peptides around the 136-mer fibril structure, and equilibrate the system of 200 peptides for 200 ns at 310 K in the NVT ensemble. The final structure is shown in Figure 2 A. A total of 100 conformations were selected statistically from this MD for

our NEMD simulations.

Laser-induced NEMD simulation

A total of 100 independent NEMD simulations are performed for each laser property. It is useful to recall some aspects. In the NEMD simulation, a time-dependent electric field

$$E(t) = E_0 \exp[-\frac{(t-t_0)^2}{2\sigma^2}] \cos[2\pi c\omega(t-t_0)], \quad (1)$$

is applied to mimic a laser micro-pulse. Here, E_0 represents the amplitude of the electric field, σ is the pulse width, t is the time after the pulse maximum t_0, c is the speed of light and ω is the frequency. In our NEMD simulations, σ is set to 2 ps, and t_0 to 5 ps as used in FEL experiments, and only waters are coupled to the heat bath in order to maintain the temperature of 310 K with a coupling constant of 0.1 ps. This also mimics the experiment conditions, in which water is added periodically to the suspension during the irradiation process in order to prevent excessive evaporating. The equations of motion are integrated with a short time step of 0.2 fs to ensure the stability of the simulation. For each NEMD simulation of 500 ps we use 10 laser pulses with a pulse duration of 25 ps (Figure 2B and Figure 2C).

Simulation data analysis

The secondary structures are calculated using STRIDE.[55] A contact is defined if the distance between two heavy-atoms is less than 0.45 nm. A hydrogen bond (H-bond) was considered formed when the acceptor-donor distance is not more than 0.35 nm, and the acceptor-donor-hydrogen angle is not more than 30 degrees. The aggregates are also characterized by their solvent-accessible surface areas (SASA) using GROMACS tools and WAXS spectra using the Pepsi-SAXS program.[56] Unless specified, our data are averaged over 100 NEMD simulations for a given set of laser parameters.

Results and Discussion

Experimental results

Our method relying on the resonance between the laser frequency and the frequency of the amide I band of the fibril, thus determination of this wavelength is essential. The FT-IR spectra of the GNNQQNY peptide prior to fibrillation (pre-fibril state or oligomers) and after fibrillation (mature fibril state) are shown in Figure 3. Doublet structure of the amide I peaks from 1600 to 1700 cm^{-1} are common features of peptides. The FT-IR spectrum of the pre-fibril state exhibits a dominant peak (P1) at 1650 cm^{-1}, and a weaker peak (P2) at 1631 cm^{-1}. Upon fibrillation, the absorbance of the P2 peak increases and its intensity is similar to that of the P1 peak, reflecting the formation of β-sheet structure in the mature fibril. This observation has already been discussed for other amyloid fibrils.[33–36] The amide I peak at lower wavenumber is associated with the vibration of the C=O bonds in β-sheet stacked structure. Therefore, in what follows, the experimental FEL wawelength is set to 1631 cm^{-1}. For comparison, another experiment with a wavelength of 2000 cm^{-1}, where no peak exist, is also performed.

Thioflavin T (ThT) is a commonly used probe to monitor *in vitro* amyloid fibril formation. It is accepted that ThT binds to the side chain along the long axis of amyloid fibrils with a minimal binding site on the fibril surface spanned by four β-strands.[57,58] Figure 4 shows the ThT fluorescence intensity of the fibril with a concentration of 25 μM before irradiation, and after irradiation using the amide-I band specific laser frequency of 1631 cm^{-1} and the non-specific frequency of 2000 cm^{-1}. As seen, the fluorescence signal obtained by using the non-specific wavelength is very similar to that of the fibril, even at high laser power ($\leq$ 10 mJ per one macro-pulse), suggesting that the overall fibril structure is maintained. In contrast, the specific amide I specific irradiation at 1631 cm^{-1} results in a decrease of $\sim$ 85% of the fluorescence signal, demonstrating full destabilization of the fibril.

To get insights into the conformational change upon FEL irradiation, SEM analysis is performed. As seen from the SEM images in Figure 5A, the peptide forms fibrils composed of nu-

merous silk-like filaments, whose lengths are longer than 10 μm. After irradiation at 1631 cm^{-1}, the filaments have disappeared, indicating conversion to other conformations.

Having shown that the fibril structure is dissociated after FEL irradiation, we now wish to investigate the conformational change employing X-ray scattering experiment and FT-IR micro spectroscopy. For the organization of peptides, we perform WAXS experiments, and the spectra are shown in Figure 5B. The WAXS spectrum of the pre-fibril displays one main Bragg reflection at $q = 13.5$ nm^{-1}, corresponding to random peptides in the oligomers. Prior to FEL, the WAXS spectrum of the fibril shows a dominant peak at $q = 12.8$ nm^{-1} and a weaker peak at $q = 13.5$ nm^{-1}. The dominant peak corresponds to intermolecular C_α-C_α distances of 0.49 nm between the strands in the cross-β structure, while the second peak can be assigned to the random peptides in solution. Upon FEL irradiation at a frequency of 1631 cm^{-1}, the spectrum shows one single peak at $q = 13.5$ nm^{-1}, confirming full dissociation of the fibril.

To determine secondary structure composition, we performed FT-IR analysis of the fibril before and after irradiation with the laser frequency of 1631 cm^{-1}. The content of each secondary structure is calculated based on the peak intensity of amide I band: 1625-1640 cm^{-1} for β-sheet, 1650-1655 cm^{-1} for coil, 1645-1650 cm^{-1} for other, and 1655-1675 cm^{-1} for turn, and a total of 14 spectra was obtained for each system. The resulting secondary structure composition is shown in Figure 5C. In the amyloid fibrils, the population of β-sheet, coil, turn and helix is 68, 18, 14 and 0%, respectively. Upon FEL irradiation, these populations shift to 11, 30, 31 and 28%, indicating that the fibril has been converted to oligomers with dominant coil/turn structures.

Simulation results

To identify the amide I bands, we first calculate the IR spectrum of 100 structures, statistically selected from the equilibrium trajectory, by using the normal mode analysis as described in Ref.[42] The averaged IR spectrum in Figure 6 displays a dominant amide I band around 1675 cm^{-1} associated with the C=O stretching vibration in the cross-β structure, and a band around 1690 cm^{-1} associated with the C=O stretching vibrations in the turn, coil and helical structures. To identify

the resonance frequency between the amide I modes in the fibril and the laser field, we scan the frequency of the laser field, Eq. (1), in the range $\omega \in [1600 \cdots 1700]$ cm^{-1} with a step of 2 cm^{-1}, and for each value we carried out one single NEMD simulation of 25 ps duration. We find that the most significant fibril deformation after one single laser pulse occurs at 1675 cm^{-1} based on the variations of root-mean-square -deviation (RMSD), number of intermolecular H-bonds, R_g and SASA, (data not shown). This indicates that the resonance between the laser and the amide I mode associated with the C=O stretching vibration in the cross-β structure causes dissociation of the fibril. We should note that the dominant peak of the calculated amide I band is blue-shifted by $\sim$ 40 cm^{-1} compared to experiment, and this deviation is expected from molecular mechanics force fields in contrast to spectroscopic force fields.[59,60]

Having identified the resonance frequency, we carry out NEMD simulations of 500 ps on the full system. To understand the molecular response to the laser intensity, we performed 100 simulations, each for three laser intensities $E_0 = 1.5, 2.0$ and 2.5 V/nm at the specific amide I band frequency of 1675 cm^{-1}. For comparison, we also use the off-resonant frequency $\omega = 2000$ cm^{-1} with $E_0 = 2$ V/nm, and perform 100 NEMD simulations.

As a first step towards characterizing the laser-induced structural change, we show in Figure 7A snapshots of the system at 500 ps. Because the laser with frequency $\omega = 1675$ cm^{-1} is in resonance with the amide I mode of the system, the dissociation is observed in all cases after 500 ps, but the fibril is partially dissociated for $E_0 = 1.5$ V/nm, whereas the fibril is fully dissociated with $E_0 = 2.0$ and 2.5 V/nm. Clearly, full dissociation with 1.5 V/nm would occur at much longer time scale. As expected, with the off-resonant frequency $\omega = 2000$ cm^{-1}, the fibril is unaffected despite the high laser intensity $E_0 = 2.0$ V/nm.

To make a connection with experiment, we calculate the secondary structure of the sample after irradiation and the WAXS spectra during the NEMD simulations for $E_0 = 2$ V/nm and $\omega = 1675$ cm^{-1}. Averaged over all simulations between 490 and 500 ps using E_0 = 2 V/nm, the calculated β-sheet, coil, turn and helix are 5, 40, 40 and 15%, respectively. These results are in agreement with FT-IR experiments after irradiation, though small deviations are observed (Figure 8).

Looking at the time-evolution of the WASX spectrum (Figure 7B), the fibril structure is well-maintained within the first 20 ps, the peak of the spectrum being located at $q = 13.3$ nm^{-1}, very close to the peak at 12.8 nm^{-1} of the experimental spectrum (Figure 5B). Both peaks correspond to the interchain distances of 0.47 and 0.49 nm in the simulated and experimental structures, respectively. The position of the peak is shifted to $q = 11.5$ nm^{-1} at 24 ps, revealing destabilization of the core (middle) of the fibrils, and this destabilization of the β-sheets progresses towards the extremity of the fibrils (see snapshots at 26, 30 and 50 ps in Figure 7B). After 50 ps, the spectrum basically does not exhibit any specific peak, and is similar to the experimental spectrum obtained after laser irradiation, confirming full destabilization of the fibril.

The dissociation process as a function of the laser parameters is examined, and Figure 9 shows the time evolution of secondary structures obtained from the simulations using different laser intensities and frequencies. As expected, with $\omega = 2000$ cm^{-1} the secondary structures only fluctuate around their initial values. With the resonant frequency $\omega = 1675$ cm^{-1} and $E_0 = 1.5$ V/nm, the β-sheet content decays from 65% to 40%, the turn content is almost unchanged (Figure 9C), and the coil content increases from 15% to 30% during the simulations. With $E_0 = 2.0$ V/nm, the β-sheet decays from 65% to 20% within the first 50 ps (Figure 9B), and then to 10% at 500 ps. This is accompanied by a rapid increase of coil from 15% to 50% within the first 50 ps (Figure 9D) that stabilizes to 40% after 500 ps, and an increase of turn from 20% to 42% after 500 ps. At the higher laser intensity, $E_0 = 2.5$ V/nm, the coil, turn and β-sheet contents almost reach their final values after 150 ps. For the three laser intensities, the helix content (3_{10} helix) starts to increase after 250 ps and reaches a final value of 7%. These results indicate that the time evolution of secondary structure, the exception being helix, is very sensitive to the laser intensity. It is not surprising that the calculated secondary structure varies by a few percents between the two simulations and between the simulations and the FTIR experiments as each simulation reach different oligomeric structures and cannot capture all transient oligomer states present in solution.

We show in Figure 10 the time evolution of the total number of inter- and intra-molecular hydrogen bonds, SASA and R_g. Again, the off-resonant laser $\omega = 2000$ cm^{-1} does not induce

any significant changes in those quantities. With $\omega = 1675$ cm^{-1} and $E_0 = 1.5$ V/nm, the number of intermolecular H-bonds decays from 800 to 500 (Figure 10A) and both SASA and R_g increase by 30% after the first pulse (25 ps), and then these values fluctuate for the rest of the simulation. Because only the middle of the fibril is partially destabilized at 500 ps (see Figure 7A), the number intramolecular of H-bonds (Figure 10B) remains nearly constant during the simulation.

Time evolutions of the intermolecular H-bonds, SASA and R_g obtained with the higher laser intensities of 2 and 2.5 V/nm are similar, though more pronounced with the highest intensity. With time, the number of intermolecular H-bonds decreases to 25% of its initial value, SASA augments by a factor of $2-3$ (Figure 10C), R_g augments by a factor of $1.4-1.5$ (Figure 10D), and the number of intramolecular H-bonds reaches $300-400$ (Figure 10B), indicating progressive formation of disordered and expanded oligomers. This formation is characterized by oscillatory fluctuations as a response to the laser field. After each pulse, all structures tend to reassembly partially because of the competition between the van der Waals and Coulombic interactions prior to the application of the next pulse. This reflects the high plasticity of amyloid fibrils and explains why fibrils are so difficult to dissociate. It is interesting that the dissociation processes for both E_0=2 Vnm^{-1} and E_0=2.5 Vnm^{-1} are very similar. This suggests that the dissociation mechanism of the fibril induced by the resonance with the laser does not depend much on the power of the laser.

To examine the dissociation process at the residue level, we show in Figure 11 the inter-peptide H-bond maps for the case $E_0 = 2$ V/nm and $\omega = 1675$ cm^{-1}. At $t = 0$ ps, the parallel β-sheets are stabilized by five strong interchain pairs; N-N, Q-N, N-Q, Q-Q and N-Y, and six other pairs with lower populations. Upon laser irradiation, the number of contacts between the five dominant pairs is continuously reduced from its initial value of ~ 140 to $\sim 20-40$ contacts after 50 ps, but the contact pattern is maintained. This result conjointly with the snapshot at 50 ps shown in Figure 7B indicates that the early-induced laser effect is to increase the separation between peptides, but the peptides do not undergo any large conformational reorientation and translation, otherwise new contact pairs would be formed. Identical results are obtained with $E_0 = 2.5$ V/nm, further supporting that the dissociation mechanism does not depend on the laser intensity.

Finally, it is of interest to know how much the system is heated by the laser irradiation. To this end, we calculate the temperatures of the fibril and the solvent, and results are shown in Figure 12 for the laser intensity of 2 V/nm. Initially, the system is in equilibrium and the temperatures of both fibril and solvent are 310 K. After 16 ps, the intensity of the laser increases and reaches the maximum value at 20 ps (Figure 2C). As a consequence, the temperatures of the fibril and solvent increase and reach the maximum values of $\sim$ 1489 K and $\sim$ 317 K, respectively. Then, the intensity of the laser decreases and vanishes at 24 ps. Because the solvent is thermostated, thus its temperature quickly decreases to the equilibrium temperature of 310 K, and is maintained at this value until the next excitation at 50 ps. The temperature of the fibril decreases from 1489 K to 1000 K at 24 ps. This fast decrease is due to the fast energy redistribution within the fibril, which is on the picosecond timescale.[61–66] However, because the fibril is not coupled to the heat bath, so its temperature continues to drop but slowly through the coupling to the solvent, and this process takes place in a nanosecond timescale.[61–66] Indeed, at 50 ps, the temperature of the fibril is still about 500 K.

To understand whether the dissociation is induced by thermal excitation, in our previous work, we carried out an equilibrium MD simulation where amide I band of the fibril was coupled to the heat bath at high temperature of 1360 K.[42] We observed that the fibril was immediately heated, leading to the dissociation, but the conformational changes take place slowly as compared to the those obtained from laser-excitation. From this result, together with the fact that the maximum temperature of the fibril in the current work is $\sim$ 1489 K, we suggest that the laser-induced fibril dissociation process observed in the current NEMD simulations is also not due to just thermal effects but primarily due to the excitation of the amide I band vibration.

Conclusions

We have presented a joint experimental/simulation study to characterize the dissociation of the GNNQQNY amyloid fibril upon laser excitation of the amide I band of the fibril. First, we con-

struct the fibril so that its 2D and 3D structures are similar to those of experiment before FEL irradiation. Second, the intensity of the laser in the simulation is adjusted so that the simulated WAXS spectra and 2D structure are similar to those of the experiment after laser irradiation. Then, the molecular details of the transient dissociation process are revealed by the simulation.

The NEMD simulations show that the strong resonance between the laser field and the amide I vibrational band of the fibril is the cause of the dissociation. The resonance disrupts locally the intermolecular H-bond network, leading to increases in some interpeptide separations, but these peptides do not undergo large translational and orientational motions. These early perturbations that fragment a few H-bonds occur in the core of the fibrils and then propagate to the fibril extremities resulting in unstructured expanded oligomers. In this context, this mechanism is quite different from that obtained by using other methods such as ultrasound, drugs or graphene nano-sheet, where the peptides on the surface of the fibril are detached first.[28,29,67,68]

As shown above, the timescale in experiment is minutes and the length scale of the fibril is micrometers. We knowledge that we cannot perform NEMD simulations with these time and length scales due to the limitation of the current computer power. Our NEMD simulation can only capture nanosecond-time processes of nanometer-sized systems. So the main question is whether the dissociation mechanism that occurs in the simulation is the same mechanism that we observed in the experiment? We note that in the fibril dissociation mechanism caused by resonance, the two most important quantities that determine the dissociation process are the frequency of the fibril and the intensity of the laser. First, it is clear that the frequency of the fibril amide I band is almost independent of the size of the fibril. Indeed, as shown above, the frequency of the amide I band of experimental fibril is 1631 cm^{-1}, and this frequency of the fibril in the simulation is 1675 cm^{-1}, even though the size of the two fibrils is completely different. This indicates that the size of fibril should not affect the dissociation mechanism. We should stress again that the discrepancy between these two frequencies is simply due to the inaccuracy of the classical force fields in the modelling of high frequency vibrational modes. Second, if the laser intensity is high, as used in the simulation, then the amplitude of the amide I band oscillation is large, thus the H-bond network is

strongly destabilised, and therefore the fibril dissociation time is fast. Indeed, as shown above, with the intensities of 2.5 V/nm and 2.0 V/nm, the dissociation in the simulation is basically completed within 150 ps and 500 ps, respectively (Figure 9). In contrast, if the laser intensity is low then the amplitude of the amide I band is small, and therefore it will take a long time, say, on the minute timescale as used experimentally to excite the H-bond network and subsequently to dissociate the fibril. Taken together, our qualitative argument suggests that the main characteristics of the fibril dissociation mechanism that occur in experiments and simulations should be similar, and only the dissociation timescales are different.

In view of the inability of drugs to slow or reverse the cognitive impairment of AD thus far, developing non-pharmaceutical approaches against AD is now highly desirable. The ability of FEL to dissociate fibril opens up a promising approach to treating AD. Our long-term goal is to establish a method which combines FEL experiment with NEMD simulation into a framework to study the process of fibril dissociation at the molecular level. In the present study we are only able to establish a link between experiment and simulation at the beginning and the end of the process. In the next study, we plan to use the IR pump-proble method to obtain 1D and 2D transient spectra. The direct comparison between the experimental spectra and the simulation spectra will allow us to understand in detail the structural changes of fibril during the dissociation process. This work is underway.

Acknowledgment

This work has been supported by the the Department of Science and Technology at Ho Chi Minh City, Vietnam (grant 13/2020/HĐ-QPTKHCN), the “Initiative d’Excellence” program from the French State (Grant “DYNAMO”, ANR-11-LABX-0011-01, and “CACSICE”, ANR-11-EQPX-0008), and the National Institutes of Health (R01-GM079383, R21-GM097617, P30-DA035778). The content is solely the responsibility of the authors and does not necessarily represent the official views of the National Institutes of Health or other funding organizations. Computational

support from the IDRIS, CINES, TGCC centers (project A0080711440), and the Center for Research Computing of University of Pittsburgh, and the Extreme Science and Engineering Discovery Environment (CHE090098, MCB170099 and MCB180045P), are acknowledged.

References

(1) Dobson, C. M. Protein-misfolding diseases: Getting out of shape. *Nature* **2002**, *418*, 729–730.

(2) Nasica-Labouze, J.; Nguyen, P. H.; Sterpone, F.; Berthoumieu, O.; Buchete, N.-V.; Coté, S.; Simone, A. D.; Doig, A. J.; Faller, P.; Garcia, A. et al. Amyloid β Protein and Alzheimer's Disease: When Computer Simulations Complement Experimental Studies. *Chem. Rev.* **2015**, *115*, 3518–3563.

(3) Makin, O. S.; Serpell, L. C. Structures of amyloid fibrils. *FEBS J.* **2005**, *272*, 5950–61.

(4) Nelson, R.; Eisenberg, D. Recent atomic models of amyloid fibril structure. *Curr. Opin. Struct. Biol.* **2006**, *16*, 260–265.

(5) Miti, T.; Mulaj, M.; Schmit, J. D.; Muschol, M. Stable, metastable, and kinetically trapped amyloid aggregate phases. *Biomacromolecules* **2015**, *16*, 326–35.

(6) Khare, S. D.; Dokholyan., N. V. Molecular mechanisms of polypeptide aggregation in human diseases. *Curr. Protein Pept. Sci.* **2007**, *8*, 573–579.

(7) Lv, Z.; Roychaudhuri, R.; Condron, M. M.; Teplow, D. B.; Lyubchenko, Y. L. Mechanism of amyloid β-protein dimerization determined using single-molecule AFM force spectroscopy. *Scientific Reports* **2013**, *3*, 2880.

(8) Watanabe-Nakayama, T.; Ono, K.; Itami, M.; Takahashi, R.; Teplow, D. B.; Yamada, M. High-speed atomic force microscopy reveals structural dynamics of amyloid β_{1-42} aggregates. *Proc. Natl. Acad. Sci. USA* **2016**, *113*, 5835–5840.

(9) Tinker-Mill, C.; Mayes, J.; Allsop, D.; Kolosov, O. V. Ultrasonic force microscopy for nanomechanical characterization of early and late-stage amyloid-β peptide aggregation. *Scientific Reports* **2014**, *4*, 4004.

(10) Strasfeld, D. B.; Ling, Y. L.; Shim, S.-H.; Zanni, M. T. Tracking Fiber Formation in Human Islet Amyloid Polypeptide with Automated 2D-IR Spectroscopy. *J. Am. Chem. Soc.* **2008**, *130*, 6698–6699.

(11) Kim, Y. S.; Liu, L.; Axelsen, P. H.; Hochstrasser, R. M. Two-dimensional infrared spectra of isotopically diluted amyloid fibrils from Aβ40. *Proc. Natl. Acad. Sci. USA* **2008**, *105*, 7720–7725.

(12) Shim, S.-H.; Gupta, R.; Ling, Y. L.; Strasfeld, D. B.; Raleigh, D. P.; Zanni, M. T. Two-dimensional IR spectroscopy and isotope labeling defines the pathway of amyloid formation with residue-specific resolution. *Proc. Natl. Acad. Sci. USA* **2009**, *106*, 6614–6619.

(13) Cummings, J. Lessons Learned from Alzheimer Disease: Clinical Trials with Negative Outcomes. *Clin. Transl. Sci.* **2018**, *11*, 147–152.

(14) Doig, A. J.; Derreumaux, P. Inhibition of protein aggregation and amyloid formation by small molecules. *Curr. Opin. Struct. Biol.* **2015**, *30*, 50–56.

(15) Doig, A. J.; del Castillo-Frias, M. P.; Berthoumieu, O.; Tarus, B.; Nasica-Labouze, J.; ; Sterpone, F.; Nguyen, P. H.; Hooper, N. M.; Faller, P. et al. Why Is Research on Amyloid-β Failing to Give New Drugs for Alzheimer's Disease? *ACS Chem. Neurosci.* **2017**, *8*, 1435–1437.

(16) Schneider, L. A resurrection of aducanumab for Alzheimer's disease. *Lancet Neurol.* **2020**, *19*, 111–112.

(17) Cummings, J.; Lee, G.; Ritter, A.; Salbagh, M.; Zhong, K. Alzheimer's disease drug development pipeline: 2019. *Alzheimer's & Dementia: Translational Research & Clinical Interventions* **2019**, *5*, 147–152.

(18) Nguyen, P. H.; Campanera, J. M.; Ngo, S. T.; Loquet, A.; Derreumaux, P. Tetrameric Aβ40

and Aβ42 β-Barrel Structures by Extensive Atomistic Simulations. I. In a Bilayer Mimicking a Neuronal Membrane. *J. Phys. Chem. B* **2019**, *123*, 3643–3648.

(19) Tornquist, M.; Michaels, T.; Sanagavarapu, K.; Yang, X.; Meisl, G.; Cohen, S. I.; Knowles, T. P.; Linse, S. Secondary Nucleation in Amyloid Formation. *Chem Commun (Camb).* **2018**, *54*, 8667–8684.

(20) Booth, D. R.; Sunde, M.; Bellotti, V.; Robinson, C. V.; Hutchinson, W. L.; Fraser, P. E.; Hawkins, P. N.; Dobson, C. M.; Radford, S. E.; Blake, C. C. F. et al. Instability, unfolding and aggregation of human lysozyme variants underlying amyloid fibrillogenesis. *Nature* **1997**, *385*, 787–793.

(21) Waldauer, S. A.; Hassan, S.; Paoli, B.; Donaldson, P. M.; Pfister, R.; Hamm, P.; Caflisch, A.; Pellarin, R. Photocontrol of Reversible Amyloid Formation with a Minimal-Design Peptide. *J. Phys. Chem. B* **2012**, *116*, 8961–8973.

(22) Johny, M.; Vijayalakshmi, K.; Das, A.; Roy, P.; Mishra, A.; Dasgupta, J. Modulating the Phe-Phe dipeptide aggregation landscape via covalent attachment of an azobenzene photoswitch. *Chem. Commun.* **2017**, *53*, 9348–9351.

(23) Deeg, A. A.; Schrader, D. T. E.; Kempter, S.; Pfizer, D. J.; Moroder, P. D. L.; Zinth, P. D. W. Light-Triggered Aggregation and Disassembly of Amyloid-Like Structures. *Chemphyschem* **2011**, *12*, 559–62.

(24) Measey, T. J.; Gai, F. Light-Triggered Disassembly of Amyloid Fibrils. *Langmuir* **2012**, *28*, 12588–12592.

(25) Hoppmann, D. C.; Barucker, D. C.; Lorenz, D. D.; Multhaup, P. D. G.; Beyermann, D. M. Light-Controlled Toxicity of Engineered Amyloid β-Peptides. *Chembiochem.* **2012**, *13*, 2657–60.

(26) Deeg, A. A.; Schrader, T. E.; Strzalka, H.; Pfizer, J.; Moroder, L.; Zinth, W. Amyloid-Like Structures Formed by Azobenzene Peptides: Light-Triggered Disassembly. *Spectroscopy: An International Journal* **2012**, *27*, 387–391.

(27) Doran, T. M.; Anderson, E. A.; Latchney, S. E.; Opanashuk, L. A.; Nilsson, B. L. An Azobenzene Photoswitch Sheds Light on Turn Nucleation in Amyloid-β Self-Assembly. *ACS Chem. Neurosci.* **2012**, *3*, 211–220.

(28) Chatani, E.; Lee, Y.-H.; Yagi, H.; Yoshimura, Y.; Naiki, H.; Goto, Y. Ultrasonication-dependent production and breakdown lead to minimum-sized amyloid fibrils. *Proc. Natl. Acad. Sci. USA* **2009**, *106*, 11119–11124.

(29) Yagi, H.; Hasegawa, K.; Yoshimura, Y.; Goto, Y. Acceleration of the depolymerization of amyloid β fibrils by ultrasonication. *Biochim. Biophys. Acta.* **2013**, *1834*, 2480–2485.

(30) Leinenga, G.; Götz, J. Scanning ultrasound removes amyloid-β and restores memory in an Alzheimer's disease mouse model. *Sci. Transl. Med.* **2015**, *7*, 278ra33.

(31) Okumura, H.; Itoh, S. G. Amyloid Fibril Disruption by Ultrasonic Cavitation: Nonequilibrium Molecular Dynamics Simulations. *J. Am. Chem. Soc.* **2014**, *136*, 10549–10552.

(32) Man, V. H.; Derreumaux, P.; Nguyen, P. H. Nonequilibrium all-atom molecular dynamics simulation of the bubble cavitation and application to dissociate amyloid fibrils. *J. Chem. Phys.* **2016**, *145*, 174113.

(33) Kawasaki, T.; Fujioka, J.; Imai, T.; Tsukiyama, K. Effect of Mid-infrared Free-Electron Laser Irradiation on Refolding of Amyloid-Like Fibrils of Lysozyme into Native Form. *Protein J.* **2012**, *31*, 710–716.

(34) Kawasaki, T.; Fujioka, J.; Imai, T.; Torigoe, K.; Tsukiyama, K. Mid-infrared free-electron laser tuned to the amide I band for converting insoluble amyloid-like protein fibrils into the soluble monomeric form. *Lasers Med. Sci.* **2014**, *29*, 1701–1707.

(35) Kawasaki, T.; Imai, T.; Tsukiyama, K. Use of a Mid-Infrared Free-Electron Laser (MIR-FEL) for Dissociation of the Amyloid. *Journal of Analytical Sciences, Methods and Instrumentation.* **2014**, *4*, 9–18.

(36) Kawasaki, T.; Yaji, T.; Imai, T.; Ohta, T.; Tsukiyama, K. Synchrotron-Infrared Microscopy Analysis of Amyloid Fibrils Irradiated by Mid-Infrared Free- Electron Laser. *American Journal of Analytical Chemistry* **2014**, *5*, 384–394.

(37) Kawasaki, T.; Tsukiyama, K.; Irizawa, A. Dissolution of a fibrous peptide by terahertz free electron laser. *Scientific Reports* **2019**, *9*, 10636.

(38) Man, V.; Truong, P.; Derreumaux, P.; Li, M.; Roland, C.; Sagui, C.; Nguyen, P. Picosecond melting of peptide nanotube with infrared laser: A nonequilibrium study. *Phys. Chem. Chem. Phys.* **2015**, *17*, 27275–80.

(39) Man, V. H.; Pan, F.; Sagui, C.; Roland, C. Comparative melting and healing of B-DNA and Z-DNA by an infrared laser pulse. *J. Chem. Phys.* **2016**, *144*, 145101.

(40) Man, V. H.; Van-Oanh, N.-T.; Derreumaux, P.; Li, M. S.; Roland, C.; Sagui, C.; Nguyen, P. H. Picosecond infrared laser-induced all-atom nonequilibrium molecular dynamics simulation of dissociation of viruses. *Phys. Chem. Chem. Phys.* **2016**, *18*, 11951–11958.

(41) Domin, D.; Man, V. H.; Van-Oanh, N.-T.; Wang, J.; Kawasaki, T.; Derreumaux, P.; Nguyen, P. H. Breaking Down Cellulose Fibrils With a Mid-infrared Laser. *Cellulose* **2018**, *25*, 5553–5568.

(42) Man, V. H.; Derreumaux, P.; Li, M. S.; Roland, C.; Sagui, C.; Nguyen, P. H. Picosecond Dissociation of Amyloid Fibrils with Infrared Laser: A Nonequilibrium Simulation Study. *J. Chem. Phys.* **2015**, *143*, 155101.

(43) Balbirnie, M.; Grothe, R.; Eisenberg, D. S. An amyloid-forming peptide from the yeast prion

Sup35 reveals a dehydrated beta-sheet structure for amyloid. *Proc. Natl. Acad. Sci. USA* **2001**, *98*, 2375–2380.

(44) Nelson, R.; Sawaya, M. R.; Balbirnie, M.; Madsen, A. O.; Riekel, C.; Grothe, R.; Eisenberg, D. Structure of the cross-β spine of amyloid-like fibrils. *Nature* **2005**, *435*, 773–778.

(45) Nasica-Labouze, J.; Meli, M.; Derreumaux, P.; Colombo, G.; Mousseau, N. A Multiscale Approach to Characterize the Early Aggregation Steps of the Amyloid-Forming Peptide GNNQQNY from the Yeast Prion Sup-35. *PLoS Comput. Biol.* **2011**, *7*, e1002051.

(46) Yokoyama, M.; Oda, F.; Nomaru, K.; Koike, H.; Sobajima, M.; Miura, H.; Hattori, H.; Kawai, M.; Kuroda, H. First lasing of KHI FEL device at FEL-SUT. *Nuclear Instrument and Methods in Physics Research A* **2001**, *475*, 38–42.

(47) Lindorff-Larsen, K.; Piana, S.; Palmo, K.; Maragakis, P.; Klepeis, J.; Dror, R.; Shaw, D. Improved side-chain torsion potentials for the AMBER99SB protein force field. *Proteins Struct. Funct. Bioinf.* **2010**, *78*, 1950.

(48) Jorgensen, W. L.; Chandrasekhar, J.; Madura, J. D.; Impey, R. W.; Klein, M. L. Comparison of simple potential functions for simulating liquid water. *J. Chem. Phys.* **1983**, *779*, 926–935.

(49) Man, V. H.; Nguyen, P. H.; Derreumaux, P. High-Resolution Structures of the Amyloid-β_{1-42} Dimers from the Comparison of Four Atomistic Force Fields. *J. Phys. Chem. B* **2017**, *121*, 5977–5987.

(50) Man, V. H.; He, X.; Derreumaux, P.; Ji, B.; Xie, X.-Q.; Nguyen, P. H.; Wang, J. Effects of All-Atom Molecular Mechanics Force Fields on Amyloid Peptide Assembly: The Case of Aβ_{16-22} Dimer. *J. Chem. Theory Comput.* **2019**, *15*, 1440–1452.

(51) Hess, H.; Kutzner, C.; van der Spoel, D.; Lindahl, E. GROMACS 4: Algorithms for Highly Efficient, Load-Balanced, and Scalable Molecular Simulation. *J. Chem. Theory Comput.* **2008**, *4*, 435–447.

(52) Ryckaert, J. P.; Ciccotti, G.; Berendsen, H. J. Numerical integration of the cartesian equations of motion of a system with constraints: molecular dynamics of n-alkanes. *J. comput. Phys.* **1977**, *23*, 327–341.

(53) Darden, T. A.; York, D. M.; Pedersen, L. G. Particle mesh Ewald: An N log(N) method for Ewald sums in large systems. *J. Chem. Phys.* **1993**, *98*, 10089–10092.

(54) Berendsen, H. J. C.; Postma, J. P. M.; van Gunsteren, W. F.; Dinola, A.; Haak, J. R. Molecular dynamics with coupling to an external bath. *J. Chem. Phys.* **1984**, *81*, 3684–3690.

(55) Frishman, D.; Argos, P. Knowledge-Based Protein Secondary Structure Assignment. *Proteins* **1995**, *23*, 566–579.

(56) Grudinin, S.; Garkavenko, M.; Kazennov, A. Pepsi-SAXS : an adaptive method for rapid and accurate computation of small-angle X-ray scattering profiles. *Acta Cryst.* **2017**, *D73*, 449–464.

(57) Biancalana, M.; Makabe, K.; Koide, A.; Koide, S. Molecular mechanism of thioflavin-T binding to the surface of beta-rich peptide self-assemblies. *J. Mol. Biol.* **2009**, *385*, 1052–63.

(58) Wu, C.; Biancalana, M.; Koide, S.; Shea, J.-E. Binding modes of thioflavin-T to the single-layer beta-sheet of the peptide self-assembly mimics. *J. Mol. Biol.* **2009**, *394*, 627–33.

(59) Krimm, S.; Bandekar, J. Vibrational Spectroscopy and Conformation of Peptides, Polypeptides, and Proteins. *Adv. Protein Chem.* **1986**, *38*, 181–364.

(60) Derreumaux, P.; Vergoten, G. A new spectroscopic molecular mechanics force field. Parameters for proteins. *J. Chem. Phys.* **1995**, *102*, 8586.

(61) Nguyen, P.; Stock, G. Nonequilibrium molecular dynamics simulation of a photoswitchable peptide. *Chem. Phys.* **2006**, *323*, 36.

(62) Nguyen, P.; Gorbunov, R. D.; Stock, G. Photoinduced conformational dynamics of a photoswitchable peptide: A nonequilibrium molecular dynamics simulation study. *Bio. Phys. J.* **2006**, *91*, 1224.

(63) V. Botan, V.; Backus, E. H. G.; Pfister, R.; Moretto, A.; Crisma, M.; Toniolo, C.; Nguyen, P. H.; Stock, G.; Hamm, P. Energy transport in peptide helices. *Proc Natl Acad Sci U S A* **2007**, *104*, 12749.

(64) Backus, E. H. G.; Nguyen, P. H.; Botan, V.; Pfister, R.; Moretto, A.; Crisma, M.; Toniolo, C.; Stock, G.; Hamm, P. Energy transport in peptide helices: A comparison between high- and low-energy excitations. *J. Phys. Chem. B* **2008**, *112*, 9091.

(65) Park, S. Y.; Nguyen, P. H.; Stock, G. Molecular dynamics simulation of cooling: Heat transfer from a photoexcited peptide to the solvent. *J. Chem. Phys.* **2009**, *131*, 184503.

(66) Nguyen, P. H.; Park, S. Y.; Stock, G. Nonequilibrium molecular dynamics simulation of the energy transport through a peptide helix. *J. Chem. Phys.* **2010**, *132*, 025102.

(67) Yang, Z.; Ge, C.; Liu, J.; Chong, Y.; Gu, Z.; Jimenez-Cruz, C. A.; Chaia, Z.; Zhou, R. Destruction of amyloid fibrils by graphene through penetration and extraction of peptides. *Nanoscale* **2015**, *7*, 18725–18737.

(68) Sonavane, S.; Haider, S. Z.; Kumar, A.; Ahmad, B. Hemin is able to disaggregate lysozyme amyloid fibrils into monomers. *Biochimica et Biophysica Acta* **2017**, *1865*, 1315–1325.

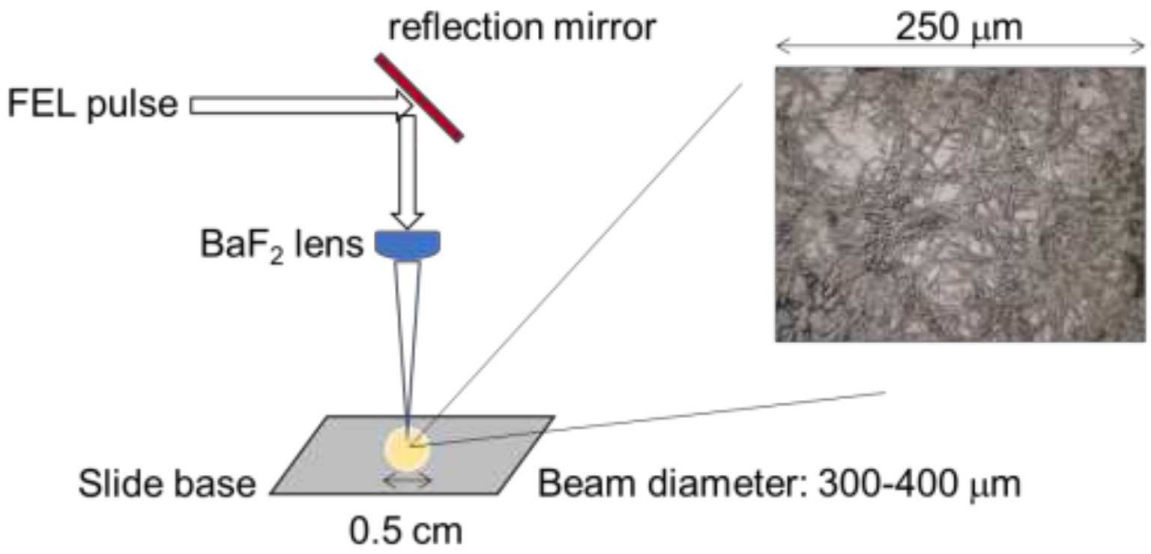

Figure 1: Schematic of the FEL experiment. The FEL pulses are generated using an electronic gun and accelerated to 40 MeV by a linear accelerator. The peptide sample was spotted on the slide base, and the laser beam was irradiated onto the sample from the vertical way by reflecting on the gold-coated mirror.

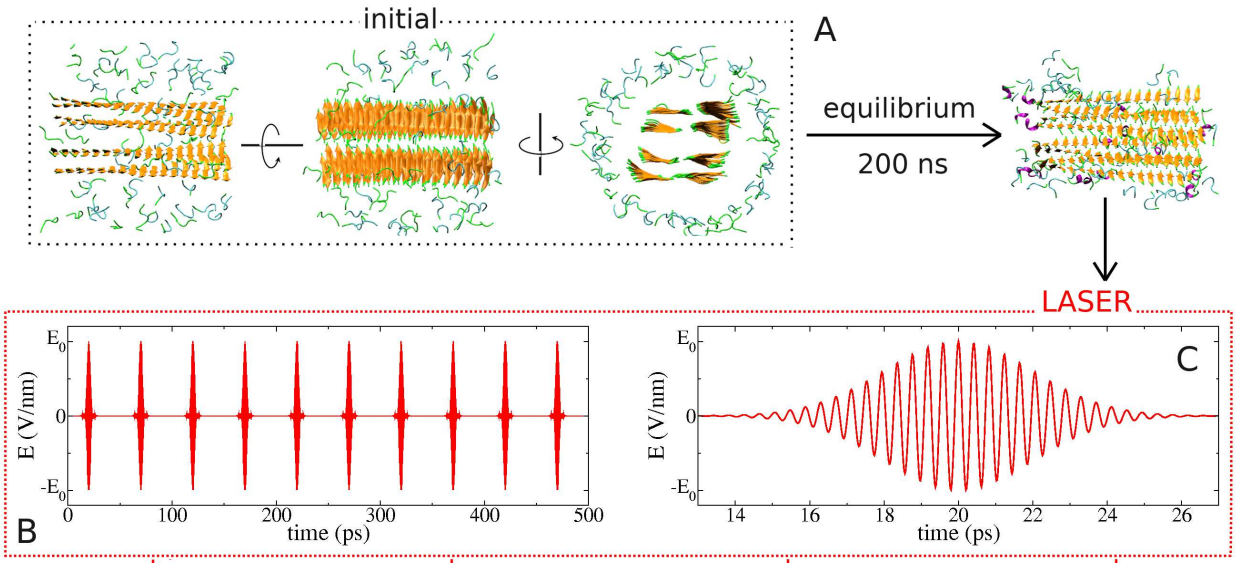

Figure 2: (A) The initial fibril structure of the simulation viewed from different angles (left), and that obtained after 200 ns of an equilibration simulation (right). Here, the β, coil, turn and 3_{10}-helix residues are shown in orange, green, blue and purple, respectively. (B) Time evolution of a chain of 10 laser pulses separated by 25 ps. (C) Time evolution of a single pulse with a duration of 25 ps.

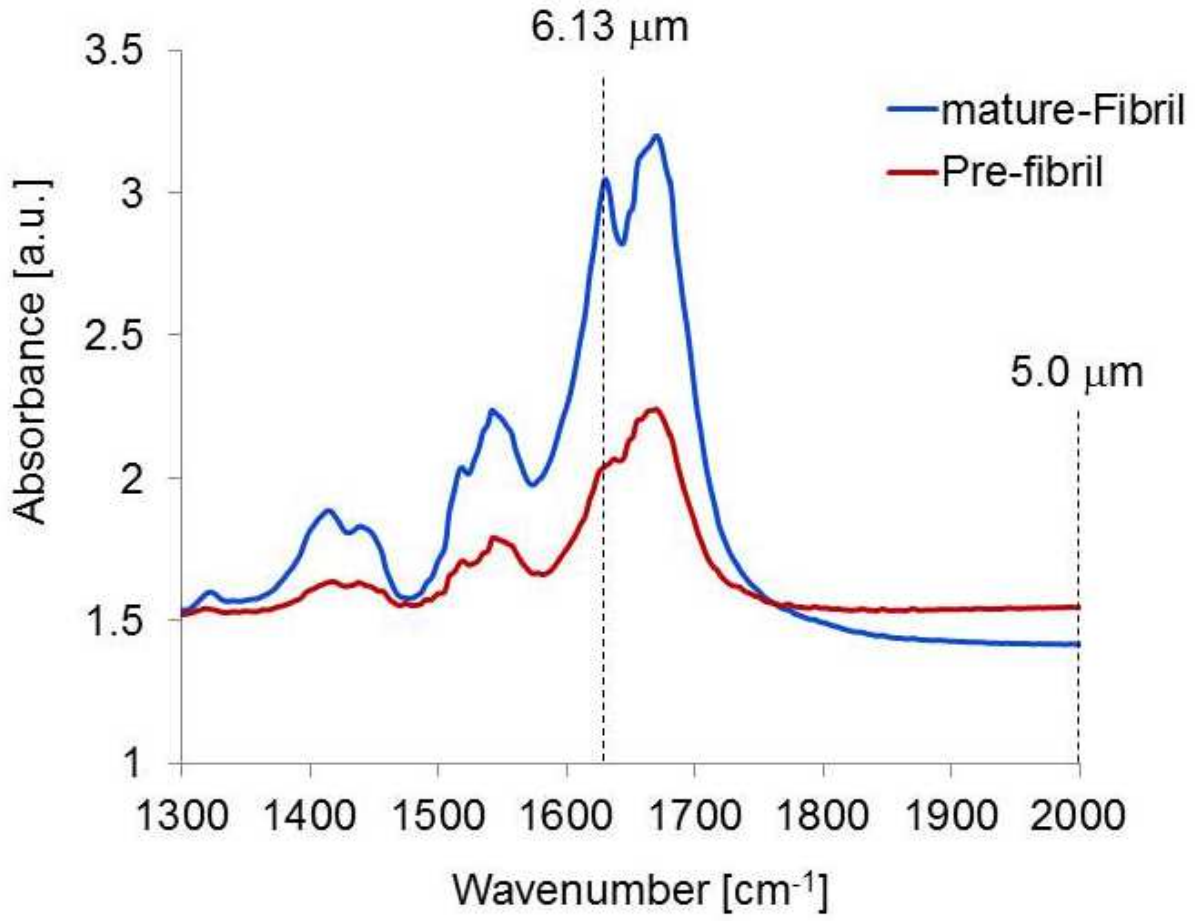

Figure 3: Infrared spectra of the pre-fibril (red) and mature-fibril (blue) of the GNNQQNY peptide system. The FEL irradiation wavelengths of 6.13 μm and 5.0 μm used in this study were marked as dotted lines.

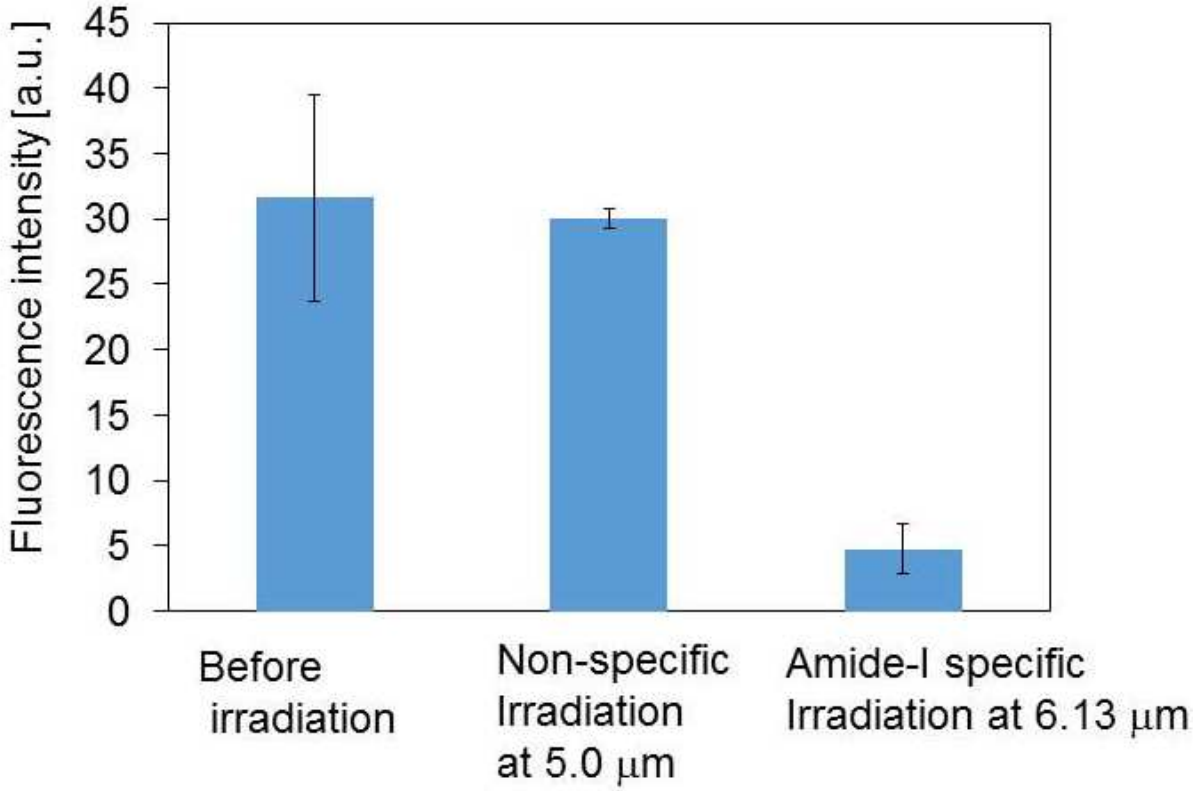

Figure 4: The ThT binding assay results of the system before irradiation and after irradiation using specific and non-specific wavelengths of 6.13 and 5.0 μm, respectively.

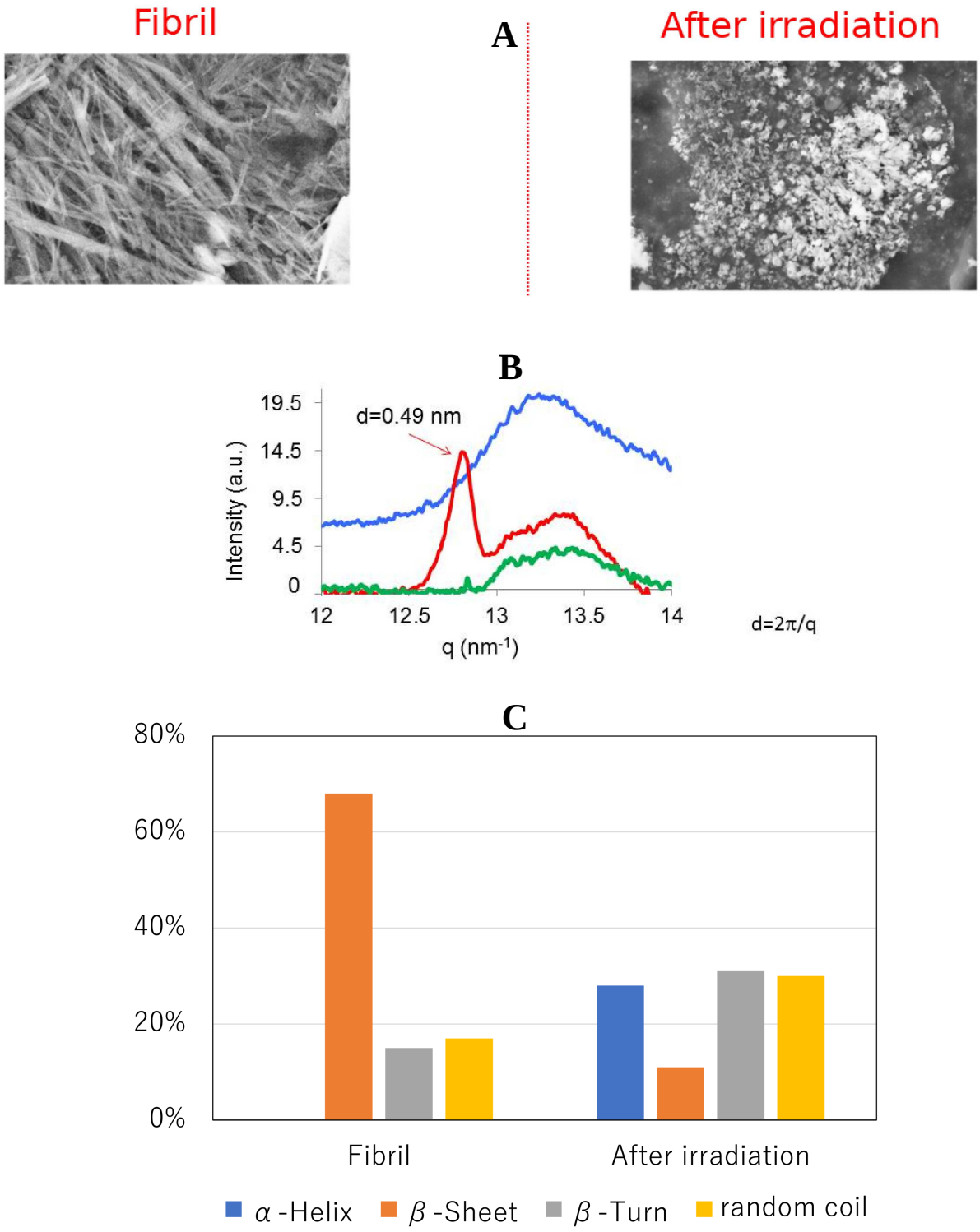

Figure 5: (A) The SEM images of the system obtained before (left) and after (right) laser irradiation. (B) The experimental WAXS spectra of the pre-fibril (blue), mature-fibril (red) and final irradiated fibril (green). (C) The population of various secondary structures of the initial fibril and final irradiated fibril. Shown are results obtained using the laser frequency of 1631 cm^{-1}.

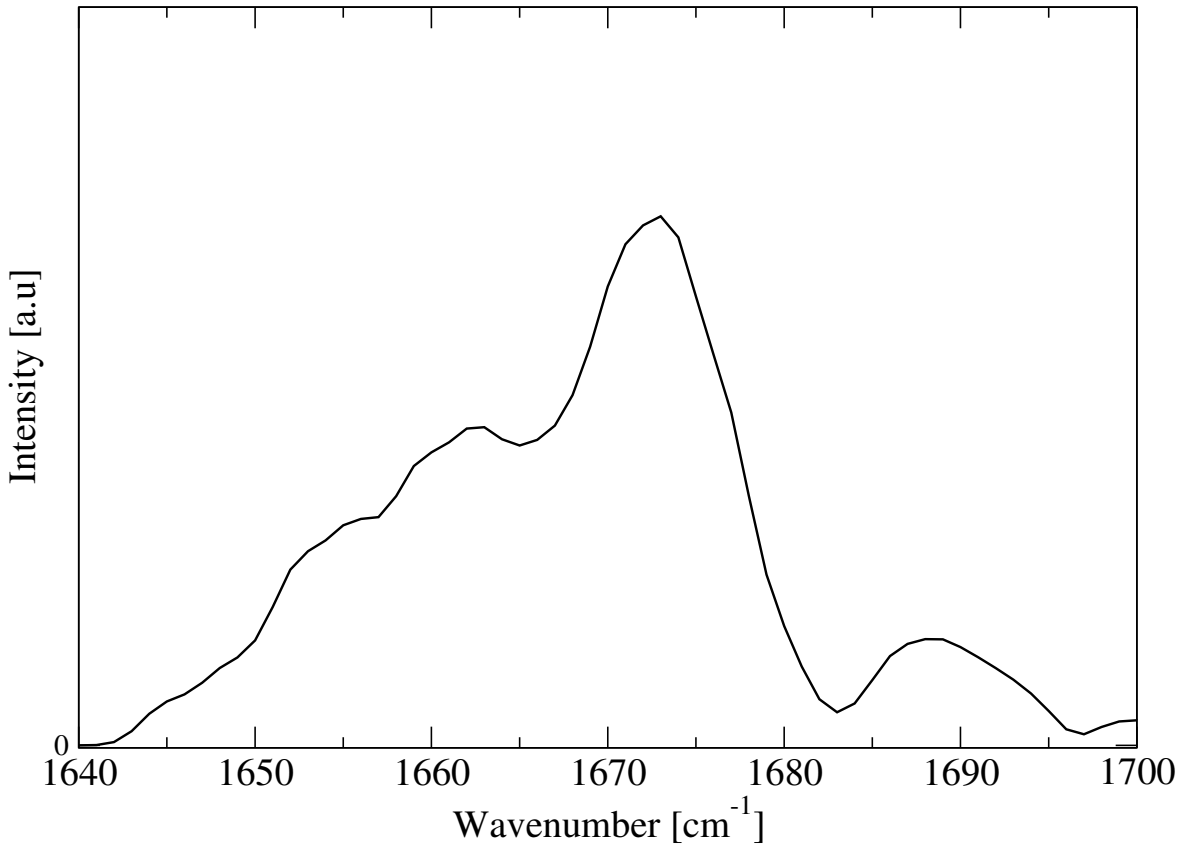

Figure 6: The averaged amide I band of the sample obtained by normal mode analysis of 100 equilibrium selected structures. The AMBER-F99SB-ILDN force field is used for the calculation.

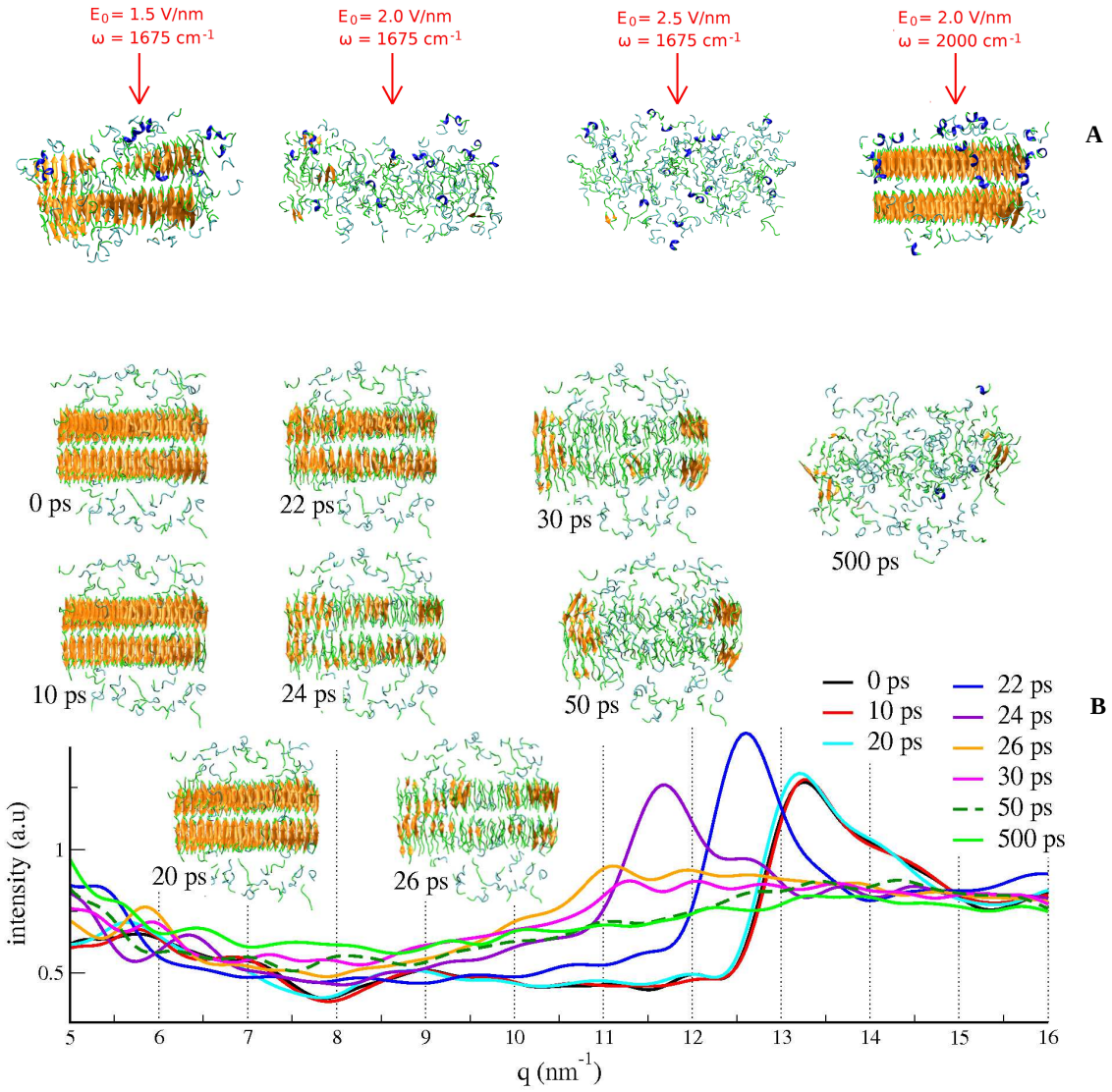

Figure 7: (A) The final snapshots at 500 ps of a NEMD trajectory simulated by using different laser intensities and frequencies. (B) The time evolution of WAXS spectra of various structures during a NEMD simulation using the laser with intensity $E_0 = 2.0$ V/nm and frequency 1675 cm^{-1}.

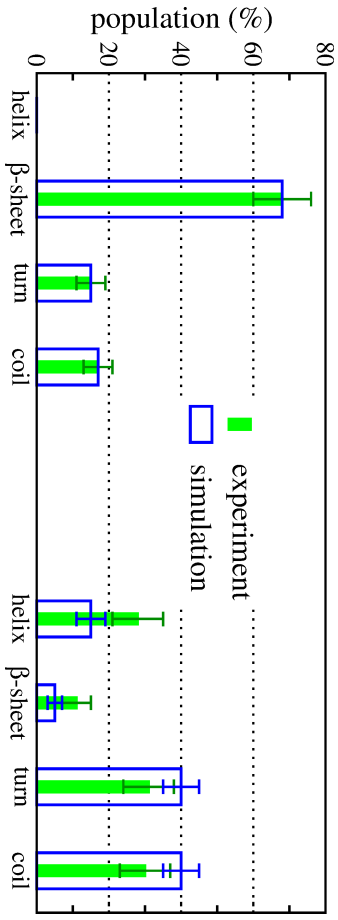

Figure 8: The populations of various secondary structures of the initial fibril (left) and final irradiated fibril (right) obtained from experiment using laser frequency of 1631 cm^{-1} (green) and from NEMD simulation using laser frequency of 1675 cm^{-1} (blue).

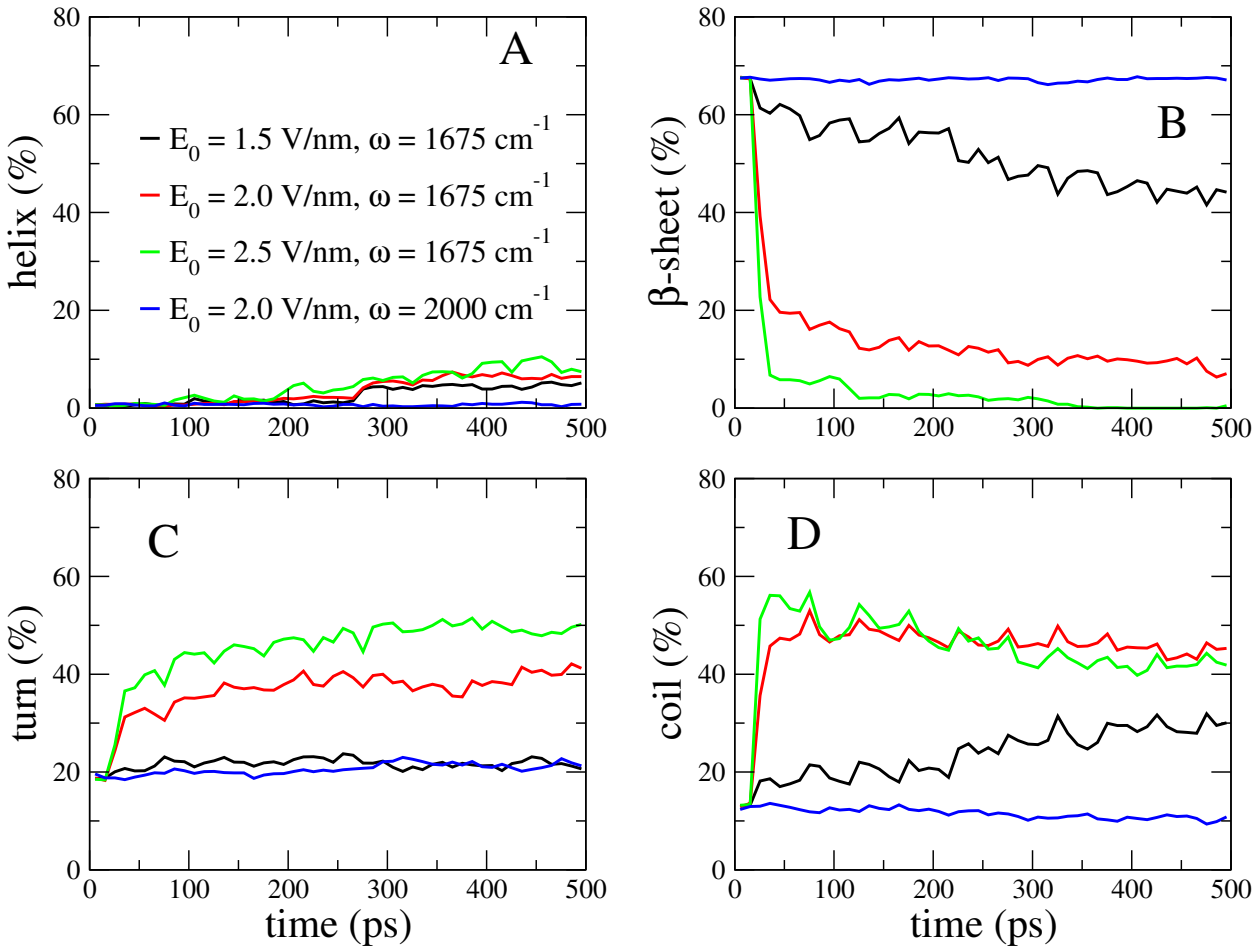

Figure 9: Time evolution of the population of various secondary structures during the NEMD simulations using different laser intensities and frequencies.

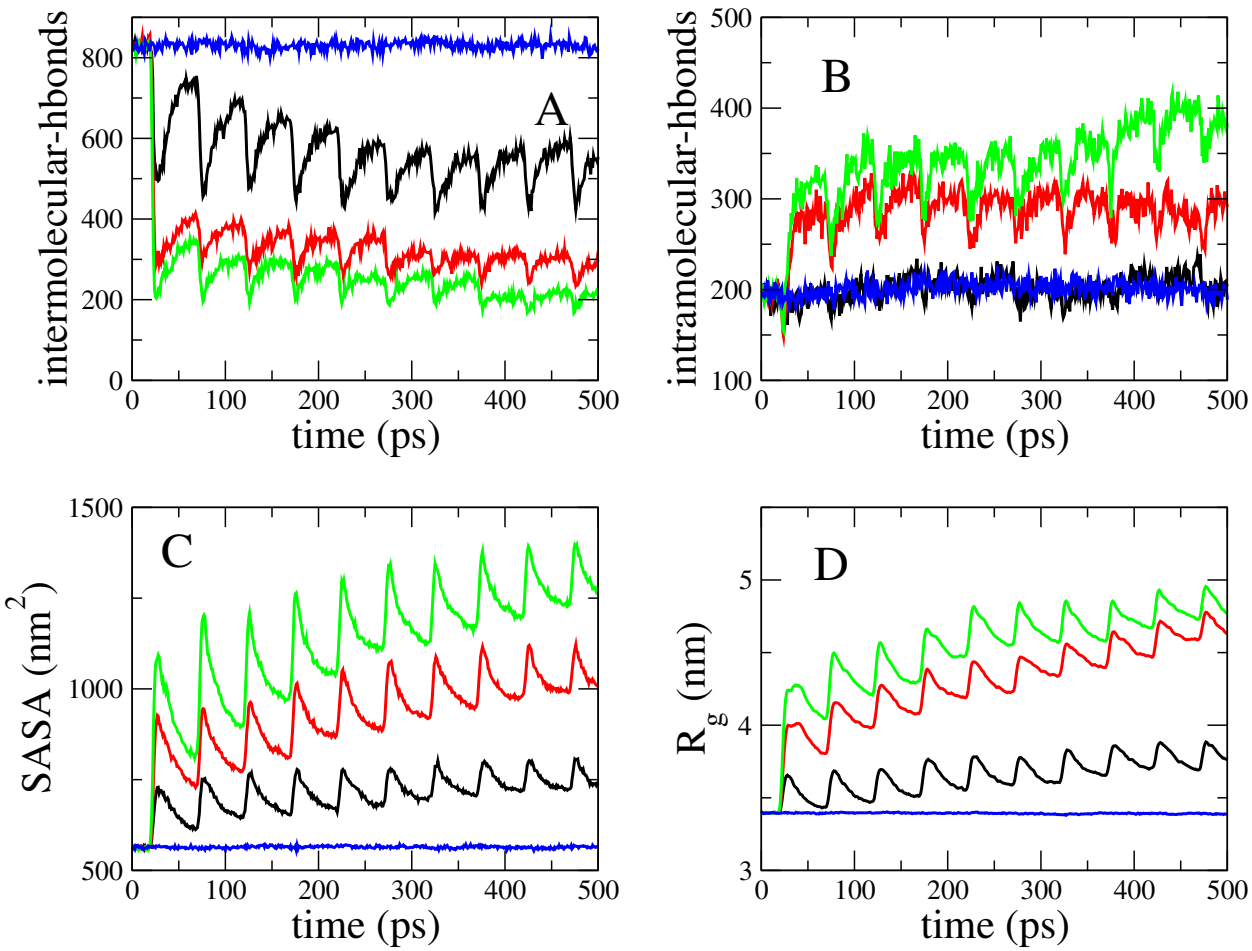

Figure 10: Time evolution of various structural quantities, including the inter- and intra-molecular H-bonds, SASA and radius of gyration (R_g) during the NEMD simulations using different laser intensities and frequencies. The colour codes are the same as in Figure 9

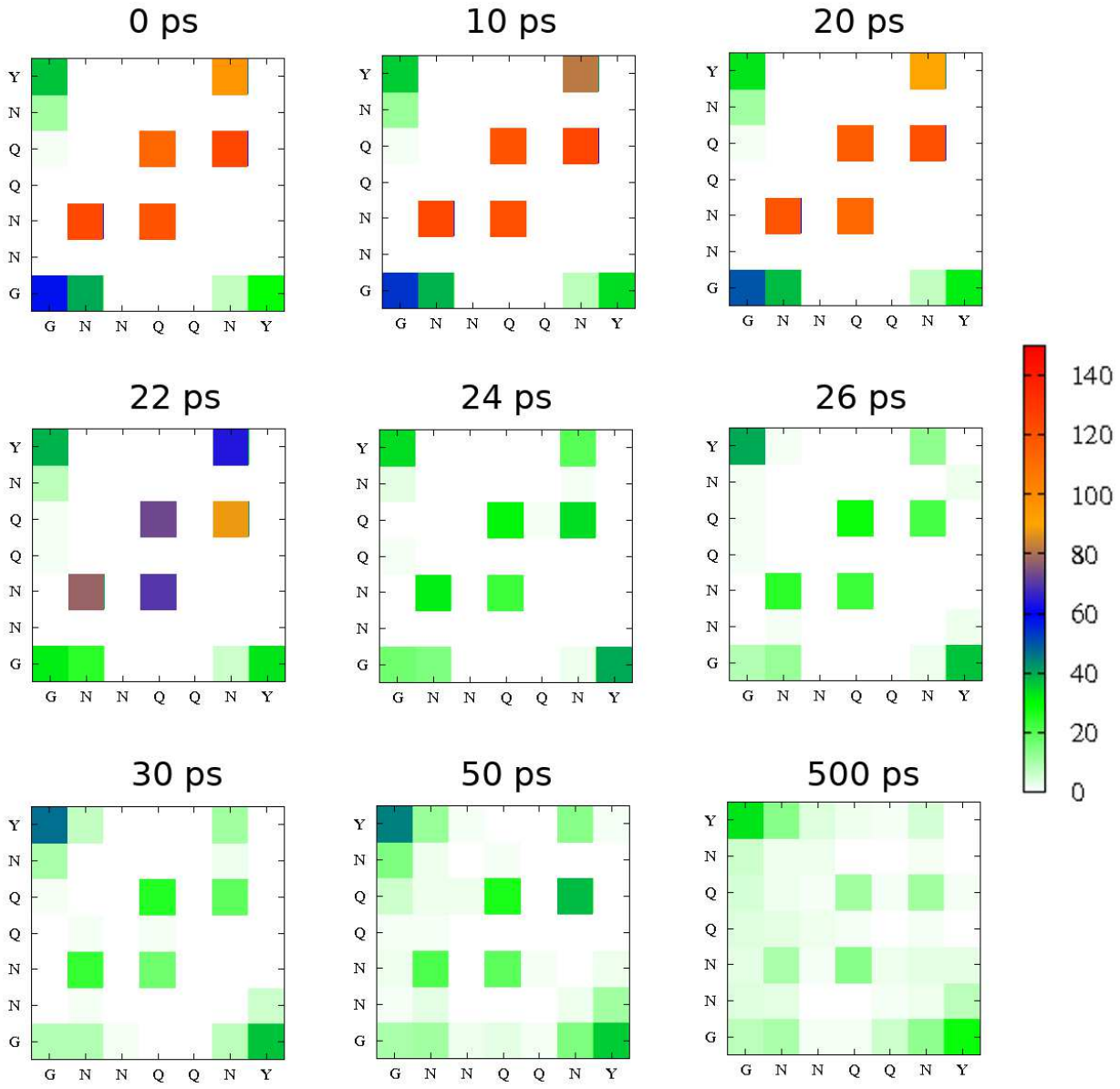

Figure 11: The intermolecular Hbond contact maps at selected times during the NEMD simulations using the laser intensity $E_0 = 2.0$ V/nm and frequency $\omega = 1675$ cm^{-1}. The colour code indicates the number of contacts.

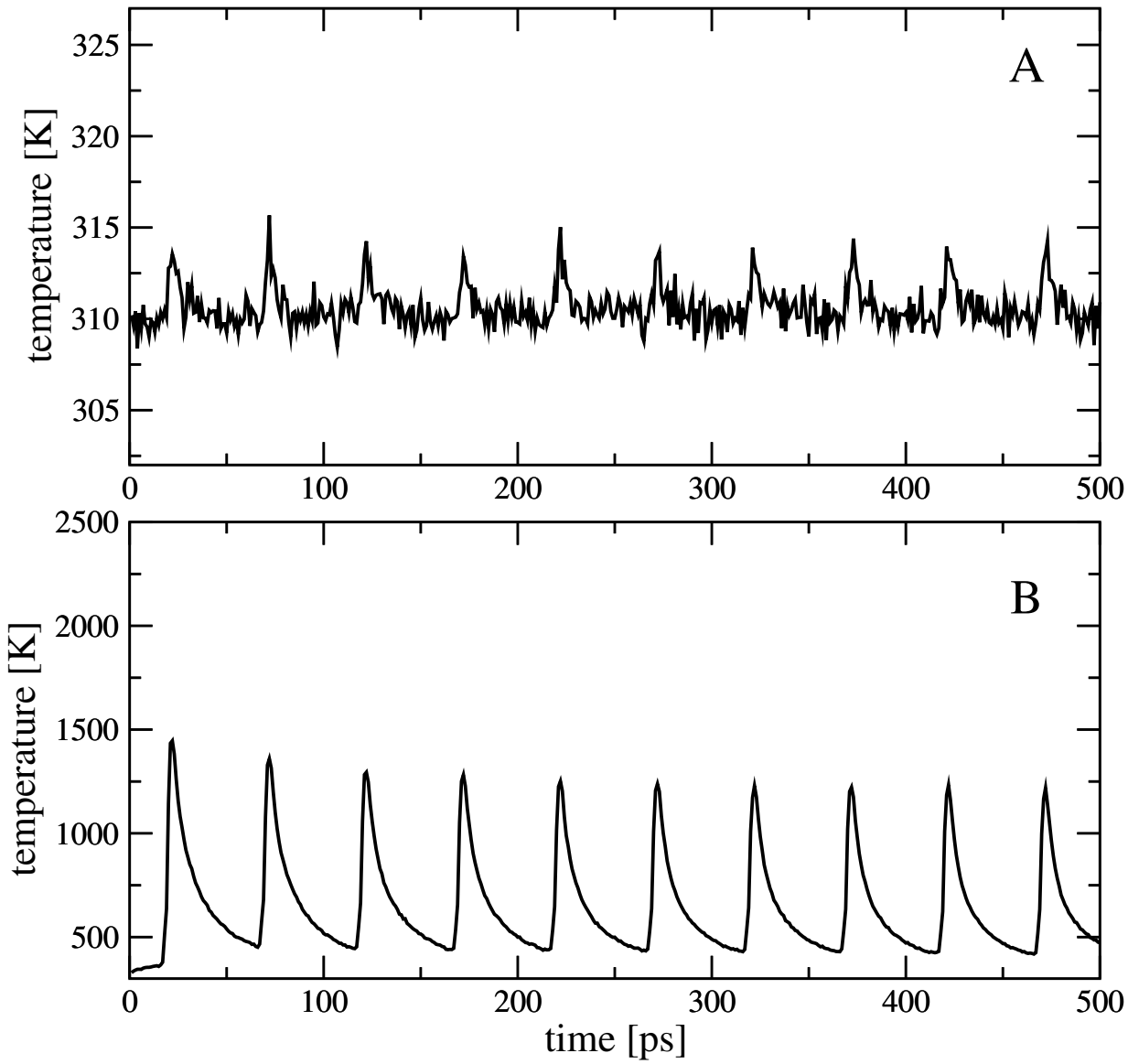

Figure 12: Time evolution of the temperature of the solvent (A) and fibril (B) during the NEMD simulation using the laser intensity $E_0 = 2.0$ V/nm and frequency $\omega = 1675$ cm^{-1}.